Cellulose (2013) 20:1691–1710
DOI 10.1007/s10570-013-9939-x

ORIGINAL PAPER

Numerical evaluation of interfibre joint strength measurements in terms of three-dimensional resultant forces and moments

Mikael S. Magnusson · Sören Östlund

Received: 4 January 2013 / Accepted: 30 April 2013 / Published online: 25 May 2013

Abstract The interfibre joint is one of the key elements in creating the strength of self-binding fibrous materials such as paper and board. In order evaluate the strength properties of interfibre joints using direct measurements, a greater understanding on how the mode of loading influences the results is desirable. The methods reported in the literature do not in general distinguish between the contributions of normal and shear stresses in the bonded region. This paper presents a numerical analysis procedure, based on the finite element method, for evaluating interfibre joint strength measurements in terms of the normal, shear, and moment loading components during testing. The target is to estimate the resultant forces and moments, that acts in the interfibre joint region at rupture, of Kraft pulp interfibre joints tested under two principally different modes of loading. The results show that for a typical interfibre joint test, modes of loading other than pure shear cannot, in general, be neglected, and are strongly dependent on the structural geometry of the fibre–fibre crosses. In addition, the resultant forces and moments were scaled in terms of the interface area and the twisting and bending resistance of the interface approximated as an ellipse to account for differences in interface area between the measurements. These scaled resultants were used to quantify how the mode of loading influences the relation between the amount of normal stress and the amount of shear stress that develop in the interfibre joint.

Keywords Fibre–fibre cross · Fibre–fibre joint · Finite rotations · Interfibre joint strength · Mode of loading · Paper mechanics · Paper strength

M. S. Magnusson (✉) · S. Östlund
BiMaC Innovation, Department of Solid Mechanics,
KTH Royal Institute of Technology, Stockholm, Sweden
e-mail: mima@kth.se

Introduction

In order to tailor the properties of fibrous network materials such as paper and board, it is essential to understand how the properties of the interfibre joints (which transfer the load between the fibres) affect the macroscopic behaviour of the material, but in order to understand the mechanical behaviour at the microscopic level, there is a need for methods that give detailed information on the failure behaviour of the interfibre joints. The methods reported in the literature do not take into account the mode of loading, and hence do not separate the measured strength values into shear and normal components. The objective of this paper is to develop an evaluation procedure to analyse these load components in terms of resultant shear and normal forces as well as the resultant peeling, twisting, and tearing moments of the joint region during loading and at rupture. Since the size of

the joint region influences the values of the resultants, the resultant forces were scaled by the overlap area and the resultant twisting and opening moments were scaled by the twisting and bending resistances, respectively, as determined by approximating the joint region by an ellipse. The present paper aims at providing a method for evaluation of the resultant forces and moments that act in interfibre joints at failure, aiming at a failure criterion in future studies.

Pulp fibres prepared for paper making are very complex and have a hierarchical structure composed of crystalline cellulosic micro-fibrils embedded in an amorphous matrix of hemicellulose and lignin (El-Hosseiny and Page 1975). These fibrils may vary considerably in orientation from fibre to fibre. The pores in the fibre walls as well as the natural curvatures and kinks (dislocations along the fibre) also contribute to the heterogeneity of the material. These fibres form chemical bonds when wet-pressed and dried in large networks, as in a paper machine. These regions of bonding (called interfibre joints) transfer the load between the fibres in the network structure. To measure experimentally the mechanical response of the individual interfibre joints, the typical approach is to test individual fibre–fibre crosses, though it should be accentuated that the properties determined during interfibre joint testing do not necessarily resemble the properties encountered in sheets, since these properties will also be affected by the manufacturing conditions undergone by the fibre network in, e.g., a paper machine. However, the interfibre joint strength values determined here are not directly intended for the prediction of the mechanical properties of paper from the individual bond properties, but for analysing the state of the loading conditions at rupture in interfibre joint strength testing, since the conventional interfibre joint strength testing methods have previously failed to differentiate the mode of loading.

Previous studies

Interfibre joint strength measurements

When measuring the individual interfibre joint strength, testing is typically carried out using a fibre–fibre cross structure. This was first reported by Mayhood et al. (1962) and later by Schniewind et al. (1964), McIntosh (1963), Mohlin (1974), Stratton and Colson (1990), Thorpe et al. (1976) and Button (1979). The general method is that one of the fibres (hereafter called the crossed fibre) is fixed onto the testing frame at both ends while the other (hereafter called the loaded fibre) is fixed at one end to a piston (or something similar) that is moving relative to the testing frame. In the conventional shearing type of loading, the direction of loading is in the direction of the axis of the loaded fibre. It is then generally assumed that the ultimate force of the tested specimen, normalised to the degree of bonding or to the overlap area, is the interfibre joint shear strength. However, the specimen tested is actually a structure in which the interfibre joint in general is subjected to a mixed mode of loading due to large rotations, e.g., the constituent fibres twist and straighten as they deform prior to rupture. The structural response characterised by the load-displacement curve of the piston is therefore influenced by the specimen geometry and the material properties of the constituent fibres. For example, depending on the experimental set-up, the fibres may twist during deformation and the normal forces that develop in the fibre–fibre interface will influence the result and should not be neglected.

Button (1979) used a finite element analysis and linear elastic fracture mechanics to analyse cellophane lap joints, and evinced a geometric dependency and concluded that it was better to represent the interfibre joint strength by the force at rupture per joint length. However, Magnusson et al. (2013) applied similar geometric normalisations (in terms of the rupture force per overlap area, width, and length of the joints), but in their results, neither parameters were exclusively more successful at reducing the variations of the interfibre joint strength between individual fibre–fibre cross tests measurements. Torgnysdotter et al. (2007) also used the finite element method (FEM) to study the influence of the distribution of the actual chemical bonding in the contact region. They found that it had little influence on the structural response of a fibre–fibre cross, but the specific distribution of the chemically bonded regions certainly affected the stress distribution in the fibre–fibre interface.

In another study on interfibre joint strength, Thorpe et al. (1976) determine an analytical expression for the strain field in the fibre surface bonded to a shive and calculated the load per unit elongation of the bonded area. Their model, which was based on small deformation linear elastic plate theory, shows that the stresses are confined to the edges of the bonded region, resulting

in a nonuniform stress distribution, but the model did not take into account the large rotations that normally occur when testing individual fibre–fibre crosses.

Recently, a novel method for making and manipulating fibre–fibre crosses using a micro robotic grip system was presented by Saketi et al. (2011). Their method allows preparing fibre–fibre crosses in a controlled manner, in terms of the crossing angle and shape factor, but, unfortunately, no measure of the force during testing was reported. This could prove to be of great value since the variability in fibre–fibre cross geometries has a large impact on the prevailing state of loading in the interfibre joint, as is quantified in this paper. Also, new methods for testing interfibre joints in load directions other than shear have been introduced recently. Fischer et al. (2012) report on joints tested in a Mode III type of loading and Schmied et al. (2012) report on joints tested in a Mode I type of loading, using atomic force microscopy.

In this paper, an analysis procedure is presented that takes into account the structural geometry of each individual fibre–fibre cross specimen to allow for a better approximation of the loads in the bonded region at rupture. By evaluating fibre–fibre crosses with natural variations in geometry and tested in two distinctly different global modes of loading, information on the resultant forces and moments that transfer the load between the fibres is obtained which, to the knowledge of the authors, is a problem previously unattended in the literature.

Experimental evaluation

A procedure for preparing and testing fibre–fibre crosses is developed in Magnusson et al. (2013), where two distinctly different loading conditions were applied: the conventional shearing type of loading, and a peeling type of loading. In this paper, further evaluation of these specimens will elaborate on the actual loading conditions that prevail in the interfibre joints at rupture in order to characterise the states of loading between the two fundamentally different ways in which the load was applied.

In the evaluation, the experimental measurements were treated as a structural response dependent on an unknown stiffness in the fibril direction and a combination of normal and shear stress components. Information on the structural geometry was gathered from microscope images of the specimens and wall thickness and micro-fibril angle from a transmission ellipsometry measurement. This information was used to relate the measured structural response to the response of a structural model of the fibre–fibre cross based on the FEM. The model was then used to evaluate the components of the interface loading in terms of resultant forces and moments in various modes of loading. The modes of loading could macroscopically be attributed to peeling, shearing, and tearing modes of rupture, as is customary in fracture mechanics, as illustrated in Fig. 1.

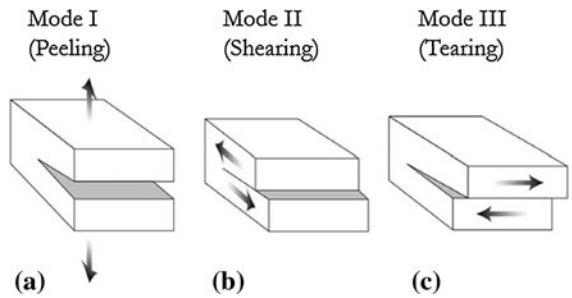

Fig. 1 Illustration of **a** peeling **b** shearing and **c** tearing modes of crack surface displacements referred to as Mode I, Mode II and Mode III type of loading, respectively

Mechanical testing

Here, fibre–fibre crosses from Kraft pulp fibres with kappa number 31 were prepared and tested according to (Magnusson et al. 2013) using a nominal drying pressure between 0.7 and 2.6 kPa, although the influence of drying pressures of such magnitudes was shown (Magnusson et al. 2013) not to influence the strength of the interfibre joints. The fixation of the fibres onto the specimen holder was achieved by using a cyanoacrylate adhesive that was viscous enough to flow all the way to the edge of the specimen holder and then stop (giving a well defined boundary for the subsequent mechanical analysis). By using liquid adhesives, the specimen could be considered at rest, and hence, minimising any handling of the specimen during the mounting process and thereby reducing possible premature deformation and damage to the fibre–fibre cross specimen. Prior to testing, micrographs which were to be used to map the geometry of each individual structure tested were taken of the specimen using a stereo microscope, see Fig. 2. The testing was conducted at a constant displacement rate of 3 μm/s. The load-displacement response (or structural response) of the point of applied loading was

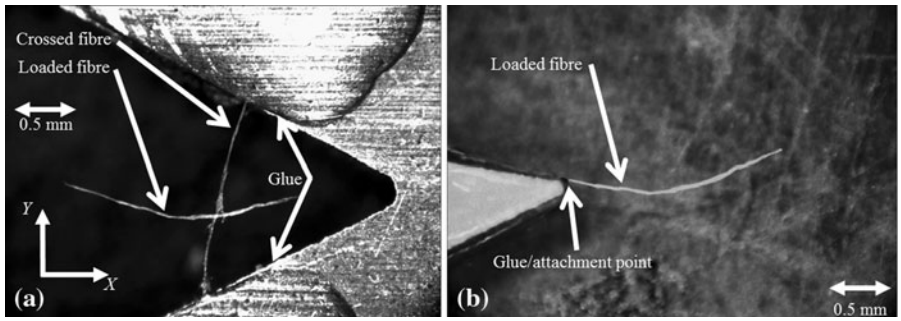

Fig. 2 Typical micrograph of **a** fibre–fibre cross glued to the specimen holder with the crossed and loaded fibres, the glue and the global coordinate system, $X - Y$, and **b** the loaded fibre after testing

recorded for each specimen. After testing, a micrograph of the loaded fibre was captured so that the attachment point of the adhesive (indicated in Fig. 2) on the loaded fibre could be back-calculated by comparing the contour length of the loaded fibre before testing and the contour length of the loaded fibre from the attachment point to the end of the fibre after testing. Hence, it was assumed that the deformation of the fibres were purely elastic, since the force that ruptured the interfibre joint was at least one order of magnitude lower than the force required to rupture the fibres (Burgert et al. 2003).

It should be noted that the mechanical testing was not done in a controlled climate, which could produce errors in the measurements, but the main focus of this study was to develop means of evaluating multi-axial load components in the fibre–fibre interface rather than another set of experimental data of joint strength with a certain statistical distribution. However, the climate was monitored for each test and the fibre–fibre crosses were tested immediately after preparation to prevent the effects of varying humidity. The climate for each evaluated specimen is tabulated in the "Appendix", Table 3.

Two distinctly different loading conditions were obtained in Magnusson et al. (2013) by simply reorienting the specimen holder prior to attaching the loaded fibre to the grip system. This allowed for experimental testing in the global *Z*-direction (the conventional interfibre joint "shear test" being loaded in the global *X*-direction).

Structural characterisation of the cell wall

The cell walls of pulp fibres are often represented by four major layers: the primary wall and three secondary layers (with varying micro-fibril angles) S_1,S_2 and S_3, as illustrated in Fig. 3.

The secondary layers, S_1,S_2 and S_3 are composed of cellulosic micro-fibrils in a lignin and hemicellulose matrix and the micro-fibrils are wrapped helically [in a Z-helix (Neagu et al. 2006)] around the longitudinal *x*-direction of the fibre at the micro-fibril angle ψ. The S_2 layer comprises 80–95 % of the fibre cell wall (Page 1969) and, thus, is assumed to dominate the mechanical behaviour of the fibre material. To determine the

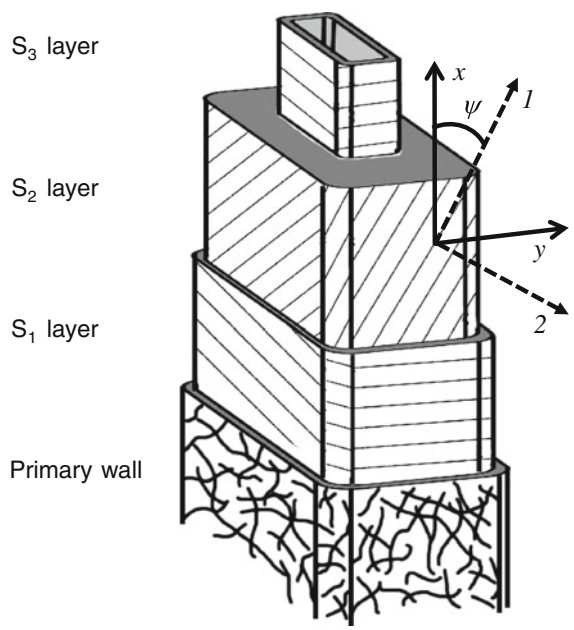

Fig. 3 The layered structure of a single pulp fibre, the layers of the cell wall are indicated in the figure. Also the local coordinate system $x - y$ and the principal coordinate system 1–2, defined by the micro–fibril angle, ψ, are illustrated for one of the fibre wall layers

fibre wall thickness, t, and the micro-fibril angle, ψ, of the S_2-layer, microscopic transmission ellipsometry (Ye and Sundström 1996; Ye 2006, 2007) and (Ye et al. 1994), was conducted on both fibres for each measured fibre–fibre cross. Micrographs were taken on a fibre segment oriented along the x-axis in the image plane. The transmitted light was first filtered to wavelengths of 470 and 540 nm using band pass filters with band widths of 40 and 50 nm, respectively, using an Olympus U-POT polariser and an Olympus AN360-3 analyser. The subsequent analysis of the micrographs was based on the assumption that the transmitted light passes through a path of the fibre that can be modelled as a simple double-walled structure consisting of two identical linear retarders in series with perpendicular polarisation angles. By collecting intensities from the corresponding measurement points in a fibre segment, for each filtered light source and each polarisation angle that was measured, and by assuming birefringence n_1–$n_2 = 0.05$ (Page and El-Hosseiny 1974), the cell wall thickness and the micro-fibril angle were estimated using the concept presented by Ye et al. (1994). It should be noted that, in the analysis of the fibres, positive (but close to zero) microfibril angles were sometimes obtained (corresponding to a S-helix), as seen in Table 4, which is not physical, and are most likely due to uncertainties in the method or to misalignment of the fibre axis during the ellipsometry. However, the effect of such small angles is negligible as they are almost in the direction of the fibre axis.

Structural analysis of the load-displacement response

In order to estimate the state of loading in the interfibre joint at rupture, specimen specific structural parameters such as the geometry together with the structural responses of each specimen were taken into account by developing a numerical model based on the FEM.

Geometric discretisation

Here, the objective was to obtain a first approximation of the state of loading of the interfibre joints by including the geometry of the fibre–fibre cross and linear elastic large rotation analysis. For this purpose, the starting point was an approximation of the centre line of the fibre–fibre cross geometry, such as shown in Fig. 4. The geometry of each test specimen was captured from micrographs using the image processing software ImageJ (Abramoff et al. 2004) and calibration of a scale bar used for microscopy analysis. About 50–100 coordinates of the centre line of each fibre were used in a typical mapping. Note that this approach only captures the plane geometry of the specimens (neglecting the depth dimension), but as the specimens were manufactured in a plane drying press, most of the natural curvatures were spanned in that plane. Also, the initial twist along the fibre direction was neglected in this study by assuming that the sides of the fibre are planar. From the micrographs of the loaded fibre (taken after testing) the point of loading (the attachment point) was back-calculated. This was done by measuring the contour length (the sum of fibre segment lengths) along the loaded fibre after testing, the segment length being the distance between two discrete material coordinates, and comparing it to the contour length of the loaded fibre before testing. After determining the point of applied loading, the tested fibre–fibre cross centre line geometry could be approximated.

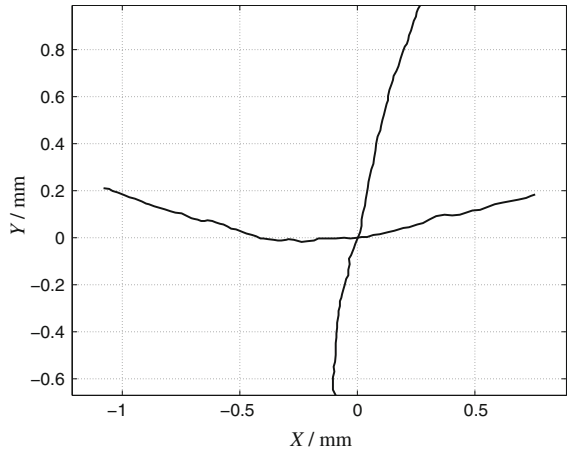

Fig. 4 Typical approximation of the centre lines of a mapped fibre–fibre cross geometry used in the structural analysis. The figure shows the *centre lines* of the fibre–fibre cross in Fig. 2

The approximated fibre–fibre cross geometries were imported into the commercial finite element software Abaqus 6.11 (Corp 2012), using the Abaqus Scripting Interface in Python. The fibres were modeled as fully collapsed volumetric bodies, using shell elements. The cross-section was assumed to be a rectangular with circular corners as illustrated in Fig. 5.

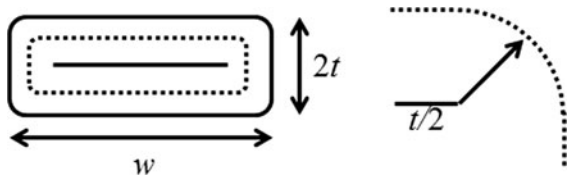

Fig. 5 Cross section geometry of the idealised fibre structure, with the midsection, marked by the *dotted line*, the wall thickness, t, and width, w. The slit in the middle is the lumen with close to zero radius, indicating a fully collapsed fibre. The radius of the corners is illustrated in the right sub-figure

The width, w, of the fibre cross section was approximated from the micrographs where the widest dimension along the fibre corresponds to the cross-sectional width. Moreover, since most fibres are in a collapsed state after drying (at least in handsheets; Lorbach et al. 2012), it was assumed that all fibres were fully collapsed. Since most fibres were in a twisted state after drying, these dimensions could easily be estimated from the micrographs. This initial twist was, however, neglected for the sake of simplicity in the model geometry.

The parameters describing the cross-section geometries, w and t, and the micro–fibril angle, ψ, were all assumed to be constant along the fibre and are tabulated in the "Appendix", Table 4 for each evaluated specimen. An idealised centre-line-geometry is shown in Fig. 6 to illustrate the geometric parameters used to describe the fibre–fibre cross specimens.

The fibre contour lengths for the crossed fibre, L_c, and the loaded fibre, L_l, that were estimated from the distances between each material coordinate measured in the microscope, give an estimate of the true lengths of the fibres. Moreover, the projected lengths, l_c and l_l, (for the crossed and loaded fibre, respectively) were calculated for the loaded fibre as the distance between the points of applied load and the joint, and for the crossed fibre as the distance between the boundary points. The tortuosity, κ, (sometimes referred to as the shape factor) of the fibres were represented by the ratio between the contour length and the projected length, giving a simple parameter for characterising the curviness of the fibres (becoming 1 for a straight fibre and $\pi/2$ for a semicircle).

$$\begin{aligned} \kappa_l &= \frac{L_l}{l_l} \\ \kappa_c &= \frac{L_c}{l_c} \end{aligned}. \tag{1}$$

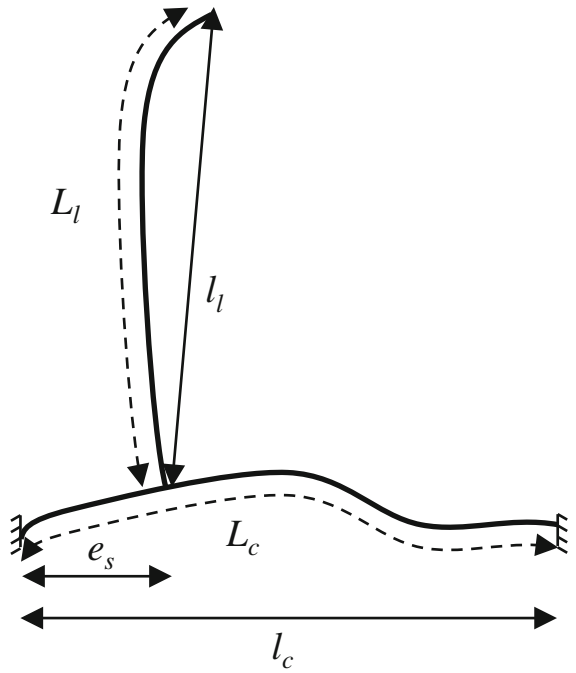

Fig. 6 Simplified centreline geometry with geometric parameters obtained from micrographs of each fibre–fibre cross specimen depicted in the figure. These could be used by the reader as an easy reference of the specimen specific geometry

In Eq. (1), the indices l and c refer to the loaded and crossed fibres, respectively. Lastly, the position of the bond is defined by the eccentricity, defined as

$$\begin{aligned} e_c &= 1 - 2\frac{e_{0c}}{l_c} \\ e_l &= 1 - 2\frac{e_{0l}}{l_l} \end{aligned}, \tag{2}$$

where

$$\begin{aligned} e_{0c} &= \min(|e_{sc}|, |l_c - e_{sc}|) \\ e_{0l} &= \min(|e_{sl}|, |l_l - e_{sl}|) \end{aligned}, \tag{3}$$

e_{sc} and e_{sl} are the distances between the glued fibre ends and the joints as depicted in Fig. 6. The definition yields an eccentricity equal to 0 when the interfibre joint is located in the middle of the crossed fibre and equal to 1 when it is located at one of the ends of the crossed fibre. These geometric features are summarised for each evaluated specimen in the "Appendix", Table 4 as a reference for the specimen specific geometry, for the ease of the reader.

The numerical model was created by extruding the cross-section of both fibres along the initial curved

centre line on top of each other with zero clearance between the surfaces (in the sequel called the fibre–fibre interface). In this way the initial geometry of the centre line of the fibre–fibre cross is planar, even if a full three-dimensional deformation of the specimen was allowed for in the analysis. Also, since the geometry of the modelled structure is very slender, large rotations develop during deformation and the analysis requires a procedure for removing the rigid body deformation for improved accuracy and geometry update for proper evaluation of stresses and accounting for stress–stiffening. This procedure was enabled with the choice of a non-linear geometrical analysis in the solution.

Constitutive behaviour

The effects of the underlining microstructure were taken into account through the transversely isotropic material law which was applied in the rotated material coordinate system. The rotation was done in two steps. The first rotation was done from the initial element coordinate system to the co-rotational coordinate system removing the effect from the large rigid body rotations (x–y–z in Fig. 3). The second rotation was done from the co-rotational coordinate system to the material coordinate system (1–2–3 in Fig. 3) to take into account the micro fibril orientation angle.

Using Voigt notation and by defining the 2–3 plane to be the plane of isotropy, Hooke's law in terms of engineering strain and stress can be expressed in the material coordinate system as follows:

$$\begin{bmatrix} \varepsilon_{11} \\ \varepsilon_{22} \\ \varepsilon_{33} \\ 2\varepsilon_{12} \\ 2\varepsilon_{13} \\ 2\varepsilon_{23} \end{bmatrix} = \begin{bmatrix} E_1^{-1} & -v_{12}E_1^{-1} & -v_{12}E_1^{-1} & 0 & 0 & 0 \\ -v_{12}E_1^{-1} & E_2^{-1} & -v_{23}E_2^{-1} & 0 & 0 & 0 \\ -v_{12}E_1^{-1} & -v_{23}E_2^{-1} & E_2^{-1} & 0 & 0 & 0 \\ 0 & 0 & 0 & G_{12}^{-1} & 0 & 0 \\ 0 & 0 & 0 & 0 & G_{12}^{-1} & 0 \\ 0 & 0 & 0 & 0 & 0 & 2E_2^{-1}(1+v_{23}) \end{bmatrix} \begin{bmatrix} \sigma_{11} \\ \sigma_{22} \\ \sigma_{33} \\ \sigma_{12} \\ \sigma_{13} \\ \sigma_{23} \end{bmatrix}. \quad (4)$$

The non-linear equilibrium equations were solved by a quasi-static FEM, an implicit scheme was used to update the unknown displacements, and an updated Lagrangian formulation was employed to linearise the equations of motions.

The engineering constants of the transversely isotropic constitutive law that governs the fibre cell wall material were deduced from Persson (2000). Persson models the cell wall of wood cells using micromechanical homogenisation based on a finite element analysis. One model that is suggested assumes transversely isotropic material properties for the main constituents of the cell wall (cellulose, hemicellulose and lignin). The engineering constants of these are found in the literature. The micro-fibrils of the S_2 and S_3 layer are then modelled as a "multiple cellulose string" as illustrated in Fig. 7.

This micro-fibril model is assumed to build up the cell wall material (as a representative longitudinal element) which is discretised in a finite element model. The equivalent stiffness properties (averaged properties on the macroscopic scale) of the cell wall material are then derived through the simulation results and yield a transversely isotropic behaviour. Assuming an orthotropic behaviour due to rectangular (the shape being quadratic in the present study) repetitive cellulose strings (which are probably more physical) did not influence the resulting equivalent stiffness properties dramatically. Hence, an approximation of the cell wall behaviour as transversely isotropic according to Fig. 3 was considered sufficient for the present analysis, by implicitly accounting for the micromechanical representative longitudinal elements in Fig. 7.

The mean ratio between the effective stiffness coefficient in the longitudinal direction E_1 (first principal material direction) and the transverse directions E_2 (second and third principal material directions) as well as the shear modulus G_{12}, was then used as the stiffness ratios in this study. The in-plane and out-of-plane Poisson ratios, ν_{23} and ν_{12}, respectively, were taken as the average (of the results obtained by

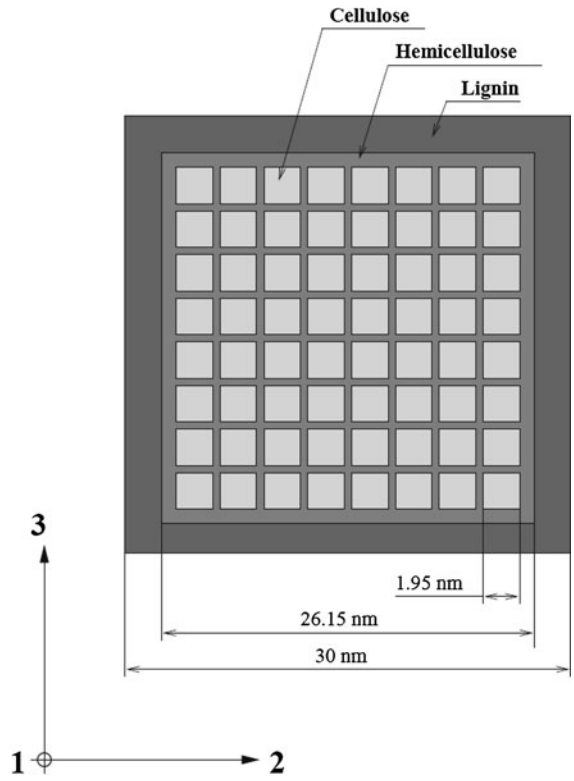

Fig. 7 Cross section of a micro–fibril modelled with multiple cellulose strings according to Fengel (1970). The picture is reproduced from Persson (2000) and the principal material directions are depicted in the figure

Persson) and assumed to be constant. From the results of this homogenisation procedure, the relations for the stiffness parameters given in Table 1 were determined and used to characterise the present fibre materials. Similar ratios are found in the literature, with ranges of $E_2 \in [E_1/2 - E_1/13]$ and $G_{23} \in [E_1/50 - E_1/9]$ in Page et al. (1977) and Groom et al. (1995), an excellent review of fibre properties can be found in Neagu et al. (2004). Here, it should be noted that it is assumed that this ratio is unaffected by the small moisture variations experienced during the testing.

By expressing the transverse tensile stiffness E_2, and the shear stiffness G_{12}, as ratios of the tensile stiffness in the micro-fibril direction E_1, the constitutive behaviour of a fibre cell wall material was governed by only one stiffness parameter and the micro-fibril angle. The tensile stiffness E_1 was used to scale the structural response of the model to the experimentally measured structural response. Note that the local material direction 1 was rotated about the 3-axis according to the measured micro-fibril angle ψ of each specimen to account for the micro-fibril angle.

Finite element discretisation

Each individual fibre–fibre cross geometry was discretised using a mesh consisting of 4-noded finite strain shell elements with reduced integration [element type S4R in Corp (2012)]. A mesh size dependency check was performed with respect to the force and moment resultants for each specimen/model to insure a reasonable precision in the results. The mesh size was considered sufficient when the differences in the resultant loading components at the interface between two consecutive runs were decreasing with mesh refinement in the contact zone, and when two significant digits were obtained. The mesh size dependency check was considered satisfactory for the purpose of the present study, however if local stress concentrations were of interest in the analysis a larger number of elements may have been needed. By using shell elements the computational cost was significantly reduced (compared to solid elements) since a fine mesh was required to resolve the stresses that develop at the edges of the contact zone in the fibre–fibre interface. A comparison between the 4-noded finite strain shell elements and 8-noded solid elements with incompatible modes was done for a reference specimen. The differences between the simulated resultant forces of the two types of elements was about 2 % of the force at rupture, but the computation time was reduced significantly using shell elements.

The interfibre joint was modelled by assuming that the entire contact area was bonded. This is of course highly unlikely as, in general, the regions close to the edge of the overlap region are not molecularly bonded (Kappel et al. 2009; Page 1960). Also, damage development could have been included in the model, but the aim of this study was to develop a first approximation of the resultant forces and moments in

Table 1 Engineering constants of the cell wall material used in this study

Coefficient	E_1	$E_2 = E_3$	$G_{12} = G_{13}$	G_{23}	$\nu_{12} = \nu_{13}$	ν_{23}
Value	E_1	$\frac{E_1}{11}$	$\frac{E_1}{23}$	$\frac{E_2}{2(1+\nu_{23})}$	0.022	0.39

the interface at rupture, and since no information on the appearance of the contact zone was known, the overlapping surfaces of the two fibres were considered to be in complete contact. To define the contact, a surface-to-surface contact discretisation, Dassault Systèmes (2012) was used, and the translational degrees of freedom of the nodes of the two surfaces were enforced in an average sense (averaging regions were centered on several adjacent slave nodes). Note that the impact of also enforcing rotational degrees of freedom had no effect on the final result.

The force and displacement in the direction of the applied loading was determined from the experiments. The loading was applied as a ramped prescribed displacement for each node on the edge of the cross section that corresponded to the point of applied loading and in the global load direction of that particular experiment (X for Mode II and Z for Mode I). The displacements in the other directions as well as the rotations of this surface were constrained. Furthermore, both rotations and translations of the ends of the crossed fibre (the glued ends) were fixed. An example of a meshed model is illustrated in Fig. 8.

Calibration of the structural model

In order to calibrate the structural model to the experimental measurements, the structural response was considered. The structural response of the numerical model was defined as the displacement component in the loading direction at the point of applied loading, δ_{FEM}, and the corresponding force, P_{FEM}, which was calculated as the sum of the nodal reaction forces in the direction of the applied load for each node on the boundary where the prescribed loading was applied. The structural model simulated the structural response until the corresponding force was equal to the measured force at rupture. The measured experimental structural response $P_{EXP}(\delta_{EXP})$ and the structural response of the model $P_{FEM}(\delta_{FEM})$ were then used to define the total work of deformation of the model and the experimental measurement. The stiffness parameter E_1 was then simply adjusted so that the residual in terms of work of deformation,

$$R = 1 - \frac{\int P_{EXP}\delta_{EXP}d\delta_{EXP}}{\int P_{FEM}\delta_{FEM}d\delta_{FEM}}, \quad (5)$$

was minimised according to criterion $R \leq 0.02$ while $|P_{FEM} - P_{EXP}|/P_{EXP} < 0.02$. Equation (5) was estimated using a trapezoidal numerical integration. This was typically achieved after only a few iterations since the structural response was almost linear close to rupture. These criteria were considered satisfactory, and the residuals were typically better. If this tolerance was not met, the stiffness parameter was simply updated again until the tolerance was achieved. It should be noted, however, that here the stiffness parameters for both the loaded and the crossed fibre were assumed identical in the model, while the microfibril angle, ψ may vary. The calibrated specimens were from the calibration procedure given stiffness parameters E_1 ranging between several orders of magnitude to minimise the residual, R, which is within a reasonable range since the stiffness of dry cellulose is at least 100 GPa (Nishino et al. 1995). Even though the range of the fitting parameter is very large, it should be emphasized that E_1 should not be thought of as the physical stiffness, but a fitting parameter at an angle, ψ, from the fibre axis. Also, a relative large range of fibre stiffnesses are to be expected [compare 3 GPa in Groom et al. (1995) and 80 GPa in Page et al. (1977)].

By this simple procedure, considering the geometry and the structural response only, the predicted force

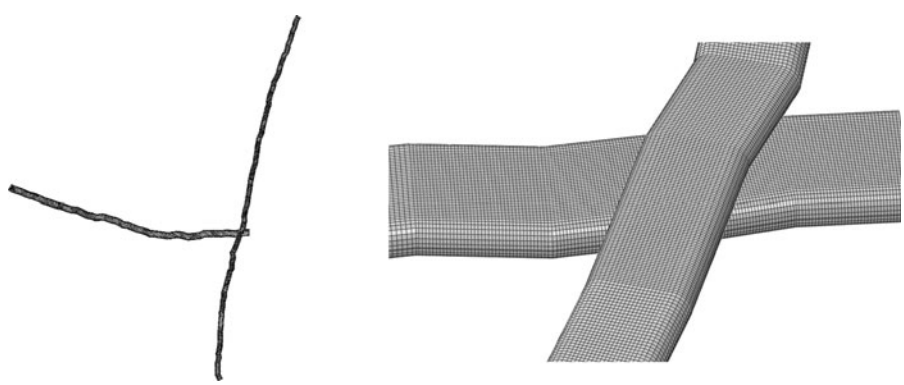

Fig. 8 Finite element model of a typical specimen to the *left* and a close–up of the fibre–fibre interface region to the *right* (the same specimen as in Figs. 2 and 4)

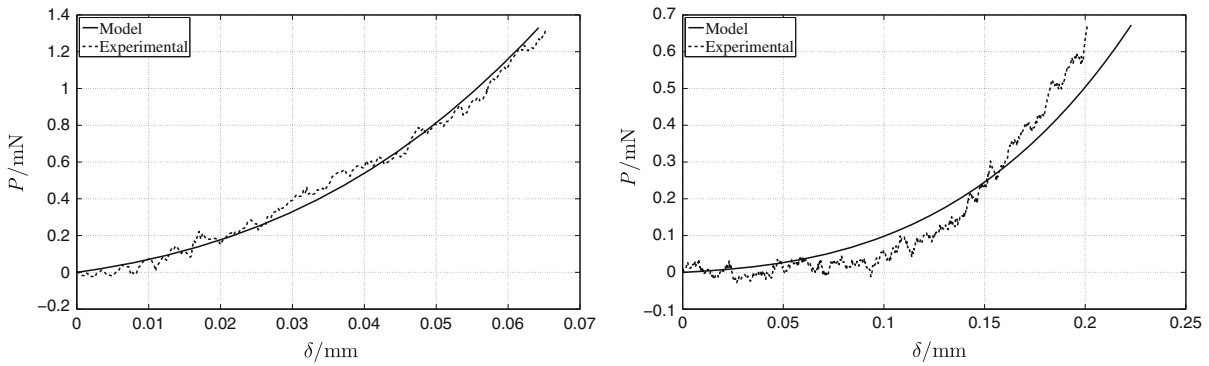

Fig. 9 Comparison between typical experimental and calibrated model structural responses for a fibre–fibre cross tested in shearing type of loading (*left*) and peeling type of loading (*right*)

displacement curve exhibited a good fit to the corresponding experimental one for the specimens. A typical example is shown in Fig. 9.

The structural response of a few specimens was not modelled well, most likely due to a significant difference in stiffness between the fibres or due to inaccuracies in the measurement of the cross section geometry. Some of these errors could of course be accounted for (like different stiffnesses for the constituent fibres or varying the cross-section along the fibres) but since more data were needed for verification and producing an unambiguous solution for these specimens, the most severe specimens were simply not included in this study. Note that by scaling the model by the work of deformation, the displacement at rupture of the model was not necessarily the same as for the experiment, but any relative discrepancy smaller than 10 % was considered satisfactory for the present evaluation. Therefore, as a first approximation, the results from the structural analysis were assumed to be valid for estimating the resultant forces and moments that are transferred by the fibre–fibre interface for each tested fibre–fibre cross.

Resultant forces and moments

Due to the complex geometry of the fibre–fibre cross specimens, the maximum force measured in the structural response cannot readily be described as the load on the interfibre joint, as it simply describes the resulting force component in the load direction of the whole fibre–fibre cross. In fact, since only a one-dimensional force sensor is used, the reaction forces in the other directions in the load cell remain unknown.

In order to estimate the resultant forces and moments in the interfibre joint, a local coordinate system was introduced and the origin was defined at the centroid of the interface region. The centroid of the interface was calculated numerically from the nodes in the contact region using a postprocessor written for Matlab R2012a (Matlab 2012).

Then a Cartesian coordinate system in the deformed configuration (at rupture) was introduced, with the first principal axis defined as the outward unit normal $\mathbf{e}_n$ of the interface surface, hereafter called the normal direction. The second coordinate axis, the shear direction $\mathbf{e}_s$, was defined to be parallel to the interface surface and orthogonal to the normal direction, in the direction of the largest force parallel to the interface surface, and thus describes the direction of the largest shear force. The third coordinate axis follows directly from the orthogonality condition $\mathbf{e}_t = \mathbf{e}_n \times \mathbf{e}_s$. It will simply be referred to as the second shear direction, but the forces in that directions will be zero due to equilibrium. The local *n*–*s*–*t* and the global *X*–*Y*–*Z* coordinate systems are shown in Fig. 10 together with the two modes of loading used in the experiments.

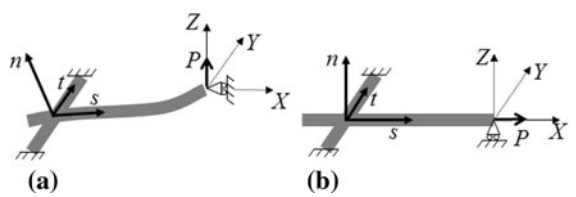

Fig. 10 The types of loading evaluated, **a** Mode I (*opening*) and **b** Mode II (*shearing*). Both the global and the local coordinate systems used are indicated in the subfigures as is the applied force, *P*

The resultant forces and moments were then expressed in the local coordinate system as resultant forces F_n, F_s, F_t and moments M_n, M_s, M_t at the centroid of the interface in relation to the directions $\mathbf{e}_n$, $\mathbf{e}_s$ and $\mathbf{e}_t$, respectively. The resultant normal force F_n, corresponds to the net force due to contact stresses in the normal direction, where a positive F_n is one pulling the fibres apart. The resultant shear force, F_s, subjects the interfibre joint to a shearing type of fracture (see Fig. 1). The resultant shear force component is what is normally discussed in the literature on rupture of interfibre joints. Moreover, the resultant in-plane moment M_n is the twisting moment about the normal axis and subjects the interfibre joint to a tearing mode, while M_s and M_t are the out-of-plane twisting moments about the s- and t-axes, respectively, that subject the interfibre joint to opening modes of loading in two perpendicular directions. These two opening moments will be presented as a resultant vector component, with magnitude

$$M_{st} = \sqrt{M_s^2 + M_t^2}. \tag{6}$$

Note that this resultant opening moment is at the angle

$$\theta = \arctan\frac{M_t}{M_s} \tag{7}$$

from the s-direction and the resultant normal force, shear force, twisting moment, and opening moment are all illustrated in Fig. 11.

Scaling the interface resultants

The magnitude of the resultant forces and moments can be used to describe the influence of the global mode of loading on the prevailing state of loading in the interfibre joint due to differences in geometry and load application, and can serve as a comparison between the two types of experiments. However, since the width of the cross section of the fibres were approximated as the local measure of the width in the microscopy analysis, something which may vary along the fibre, the overlap area in the model are not necessarily equal to the overlap area measured in the microscopy. In order to account for differences in overlap area and interface geometry between the specimens, the resultants also need to be scaled in terms of overlap area and the twisting- and bending resistances. Obviously, an elliptic contact region could have been included in the model, but since the shape and magnitude of the true contact region is unknown, in the present analysis it was considered sufficient to estimate the resultant forces and moments assuming the interface to be in full contact and scaling the resultants in the post-processing in an attempt to account for these differences. In this scaling, a simple approximation of the interface region as an ellipse was assumed. An example of such approximation is shown in Fig. 12.

Here, an ellipse tilted at an angle, η, in the s–t plane can be described as

$$\begin{bmatrix} s'(\eta,\zeta) \\ t'(\eta,\zeta) \end{bmatrix} = \begin{bmatrix} \cos(\eta) & -\sin(\eta) \\ \sin(\eta) & \cos(\eta) \end{bmatrix} \begin{bmatrix} a\cos(\zeta) \\ b\sin(\zeta) \end{bmatrix}. \tag{8}$$

with the origin at the centroid and $0 \le \zeta \le 2\pi$. The major semi-axis of the ellipse was chosen as the most distant material coordinate of the interface from the centroid and the minor semi-axis was defined as the

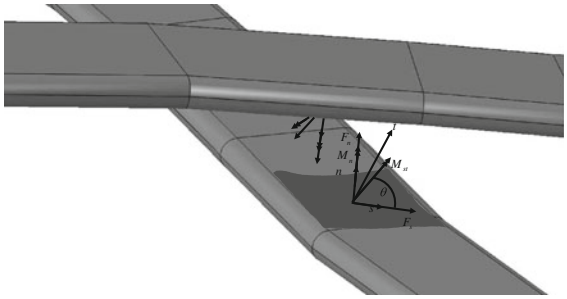

Fig. 11 The interface with the $n - s - t$ system as well as the resultant forces and moments acting at the centroid. The interface region is depicted in *shaded grey* and the fibres are translated and rotated apart for illustration purposes

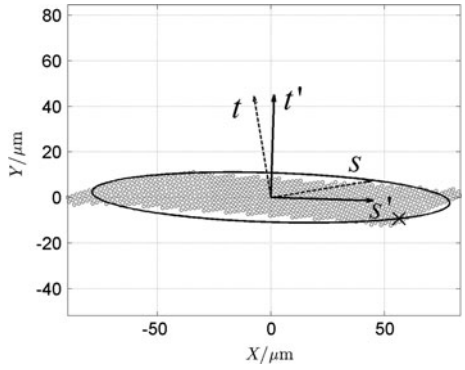

Fig. 12 An example of the contact interface (the nodes in *circles*) projected on the s–t-plane, with the s–t- and the tilted s'–t'-axes indicated as well as the elliptic surface and the point ($\times$) fulfilling Eq. (9) occurs for this particular specimen

most distant material point perpendicular to the major semi-axis. Due to local variations of the cross section geometry along the fibres, the resultants should be scaled in terms of the actual overlap area, A (measured by microscopy), which is assumed to carry the load. The area of the ellipse was defined as the measured overlap area of the interface region by adjusting the lengths of the major and minor semi-axes a and b while keeping the length ratio between them constant. Finally, the tilting angle, η, was chosen so that the number of material coordinates of the interface that satisfied Eq. (8) was maximised; that is, so that the ellipse enclosed as many material coordinates as possible. Now, by calculating the resultant forces and moment components about the major and minor semi-axes of the tilted ellipse, through rotation about $\mathbf{e}_n$ the scaled normal resultant and the scaled shear resultant of the interfibre joint at rupture could be approximated to quantify the scaled state of loading at the centroid.

The resultant normal and shear forces of the interface, F_n and F_t, were scaled by the overlap area and the rotated opening moments $M_{s'}$ and $M_{t'}$ were simply scaled by the second area moments of inertia, $I_{s'}$ and $I_{t'}$, by using the expression

$$\bar{M}_{st} = \max\left(\frac{M_{s'}}{I_{s'}}s' - \frac{M_{t'}}{I_{t'}}t'\right) \tag{9}$$

inspired by simple beam theory, where the indices s' and t' refer to the coordinates of the tilted s- and t-axes. Lastly, the resultant twisting moment M_n was scaled by the twisting resistance:

$$\bar{M}_n = \frac{2M_n}{\pi ab^2}. \tag{10}$$

Note that these quantities have the unit of stress but since they are estimated from the resultant forces and moments at the centroid and at an approximation of the interface region to obtain scalar quantities we refrain from confusing it with the actual stress distributions at the interface. These scaled measures were used in the subsequent analysis to differentiate the state of loading between the specimens with different interface geometry and overlap area.

Results

The fibre–fibre cross specimens that were evaluated in this study are summarised in Table 2 in terms of the force at rupture, P_{EXP}, the nominal overlap area, A and the resultant forces and moments obtained from the finite element analysis of each test.

From Table 2 it can be seen that for the specimens tested in a Mode I type of global loading (in the global Z-direction) the resultant force normal to the interface surface, F_n and the applied load are similar in magnitude, but not equal due to the mixed mode type of loading in the interface. The same observation can be made for the specimens tested in a Mode II type of global loading (in the global X-direction), where the magnitudes of the applied forces are similar to the resultant forces in the shearing direction, F_s. Actually, the relative difference between the applied load and the corresponding force resultant could be interpreted as a measure of the error introduced when the geometry is not taken into account: they are only on average 5 % for the shearing type of loading and 30 % for the peeling type of loading. Moreover, it is not obvious that the specimens tested in a global opening mode of loading experience a larger amount of opening moments than twist since the twist is mainly due to the geometry of the fibre–fibre cross and is naturally more difficult to control in the interfibre joint test experiment. Also, the resultant shear force is at least four times as large as the resultant normal force in these measurements.

To compare the influence of the mode of loading between the fibre–fibre cross specimens, the magnitude of the resultant twisting and opening moments are illustrated in Fig. 13.

It can be seen from Fig. 13 that the resultant opening moment is generally larger for the specimens tested in a peeling type of loading than for the specimens tested in a shearing type of loading, but that it cannot, in general, be neglected in a shearing type of loading. It can be concluded from the analysis that peeling is significant in both types of loading. Note also that in this study there were no preferences in selecting specimens with a specific geometry, but rather to account for the geometry in the analysis to obtain estimations of the resultant forces and moments that arise due to the variability of the fibre–fibre crosses in such interfibre bond strength experiments. Hence, it can be seen that the twisting moments are independent of the mode of loading as they are mainly due to the geometry of the fibre–fibre cross structure (such as the eccentricity and crossing angle of the fibres) and are of the same order of magnitude as the opening moments.

Table 2 Force at rupture, overlap area and evaluated resultant forces and moments of each specimen named by the global direction of loading *X* (for the shearing type of loading) and *Z* (for the peeling type of loading)

Specimen	P_{EXP}/mN	$A/\mu\ m^2$	F_n/mN	F_s/mN	M_n/μNm	M_{st}/μNm
X1[a]	−13.07	2,123	3.41	−13.38	0.20	0.06
X2[a]	−2.63	1,258	0.77	−2.82	−0.04	0.03
X3[a]	−1.33	600	0.19	−1.35	0.05	0.01
X4[a]	−2.46	2,265	0.64	−3.02	−0.09	0.05
X5[a]	−4.20	1,445	0.62	−4.74	−0.05	0.02
X6[a]	−6.00	1,161	1.07	−5.97	0.10	0.03
X7[a]	−4.77	552	1.54	−4.95	−0.01	0.04
X8[b]	−2.51	1,211	1.37	−2.53	0.02	0.03
X9[b]	−9.14	1,769	3.60	−8.76	−0.14	0.11
X10[b]	−0.39	348	0.17	−0.35	0.00	0.00
X11[b]	−3.17	1,558	1.68	−2.87	0.02	0.08
X12[b]	−0.46	1,369	0.29	−0.48	−0.03	0.02
X13[b]	−0.90	1,429	−1.06	−1.06	−0.04	0.02
X14[b]	−1.88	2,974	0.40	−2.17	0.09	0.02
Z1[a]	−1.54	2,560	0.94	−5.90	0.21	0.09
Z2[a]	−1.08	3,000	1.31	−2.38	−0.11	0.10
Z3[a]	−0.84	503	0.49	−3.02	0.03	0.01
Z4[a]	−0.67	1,943	0.72	−5.25	−0.10	0.11
Z5[a]	−1.02	6,946	0.33	−5.44	−0.14	0.05
Z6[a]	−0.19	1,567	0.07	−1.70	−0.01	0.01
Z7[a]	−0.46	915	0.63	−1.10	−0.01	0.01
Z8[a]	−0.19	2,690	0.12	−0.63	0.03	0.08
Z9[a]	−1.41	698	1.43	−3.79	−0.05	0.07

[a] Dried at a nominal pressure of 0.7 kPa

[b] Dried at a nominal pressure of 4.5 kPa

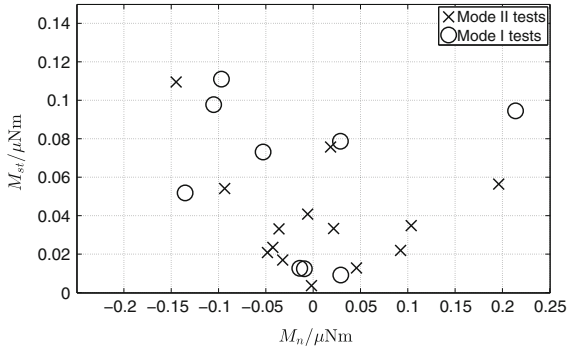

Fig. 13 The evaluated opening moments are plotted against the twisting moment for each evaluated specimen

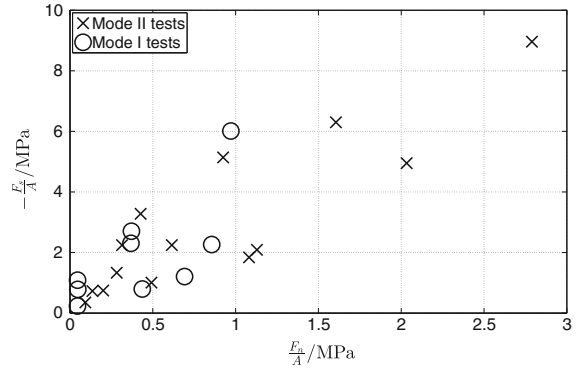

Fig. 14 The largest of the resultant shear forces plotted against the magnitude of the resultant normal forces, both scaled by the overlap area, for each evaluated specimen

Scaled state of loading

From the results of the scaling of the resultant forces and moments at the centroid of the interface, obtained by approximating the interface region as an ellipse, the scaled resultant normal force and the largest of the scaled resultant shear forces, which is between 2 and 23 times larger (depending on the specimen) than the scaled shear force in the t' axis, are plotted in Fig. 14.

From the plot in Fig. 14 no general differences are indicated between the two modes of loadings, and due to the rotation of the crossed fibre in a shearing type of loading a similar normal to shear ratio develops as for a peeling type of loading. It can be seen also that the scaled shear resultant is on average five times as high as the scaled normal resultant.

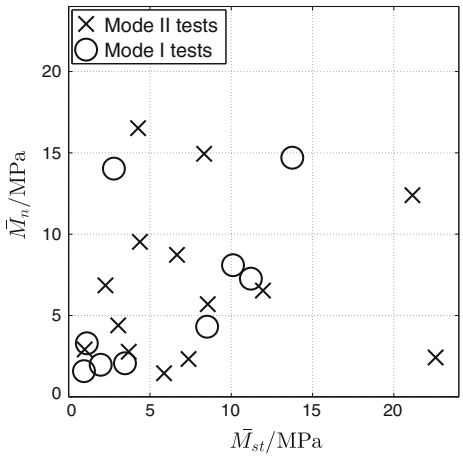

Fig. 15 The maximum of the resultant opening moments scaled by the bending resistances plotted against the resultant twisting moment scaled by the twisting resistance for the interface approximated as an ellipse

The influence on the global mode of loading can be further illustrated by plotting the scaled resultant moments, as in Fig. 15.

Note also that even though the geometry of the specimens have been taking into account, the magnitudes of the individual scaled quantities of the specimens are still varying, indicating that the scatter in interfibre joint strength is not only due to differences in the mode of loading.

Failure criteria

The results in the present analysis indicate that taking the geometry into account and estimating the resultant forces and moments transferred by the interfibre joint is not enough to remove the variations of interfibre joint strength. It is possible that the variability in strength may be physical and inherent in the interfibre joint due to variations in true bonded area or variations in bonding mechanisms (which could vary in strength) within the joint region.

Based on the present analysis the results does not indicate that there exist a simple failure criterion based on resultant quantities. However, a simple assumption that the force at rupture is equal to the average shear stress transferred by the interfibre joint could be made. But, since the shear force may be higher in a direction other than the direction of loading, a better estimation could be made using the maximum shear stress resultant, F_t. The estimated resultant forces are here normalised by the force at rupture and plotted in Fig. 16 and the error of the conventional assumption (that the shear stress is equal to the force at rupture) can be seen from the deviation of the force at rupture to the largest shear stress, F_t transferred by the joint. It is seen in the figure that the largest shear force deviates up to 23 % from the force measured in the load cell due to the geometric nonlinearity. Also, the normal forces in the interfibre joint simultaneously were between 14 and 54 % of the force at rupture, an effect which the conventional criterion is neglecting. Moreover, the mode of loading in Fig. 16 can easily be separated, as the force at rupture of the specimens tested in Mode II are close to the maximum shear force (with varying amounts of normal forces) and the specimens tested in Mode I are obviously not failing due to shear loading only. It should be noted, however, that Mode I type of loading is not governed solely by the normal force resultant (used in Fig. 16 for ease of comparison), but also by the opening moment that separates the bonded fibre surfaces.

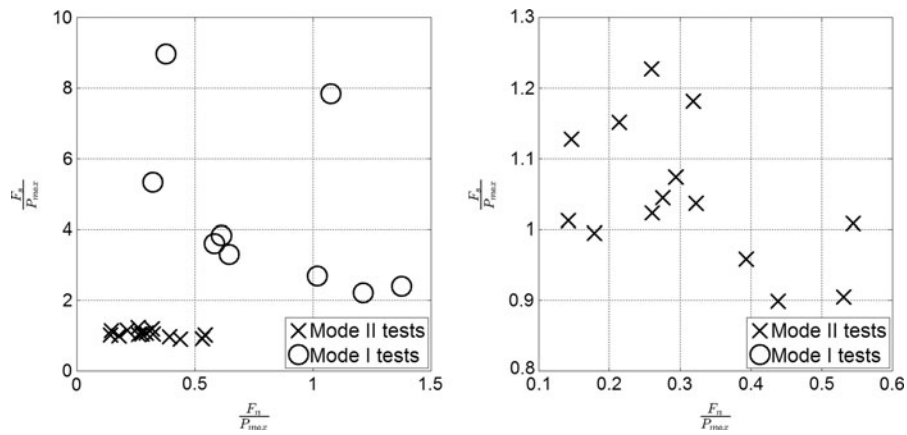

Fig. 16 The estimated resultant forces are shown for each experiment (*left*), as well the specimens tested in Mode II only (*right*)

Now, the scaled resultant forces and moment in Figs. 14 and 15 can be combined to form an effective normal stress,

$$\sigma = \bar{M}_{st} + \frac{F_n}{A}, \tag{11}$$

and an effective shear stress

$$\tau = \bar{M}_n + \frac{F_s}{A}, \tag{12}$$

respectively, using Eqs. (9) and (10). Now assume that a simple quadratic relation

$$\left(\frac{\sigma}{\sigma_0}\right)^2 + \left(\frac{\tau}{\tau_0}\right)^2 = 1, \tag{13}$$

can be fitted to the data using multivariate nonlinear regression analysis, where σ_0 and τ_0 are strength parameters. The regression resulted in $\sigma_0 = 27$ MPa and $\tau_0 = 19$ MPa. Since there is a large variability in strength between specimens, the weak specimens were avoided in order to also estimate an approximate relation for the strong interfibre joints. The boundary was determined by using specimens that were above the 95th percentile of the magnitude, $\sqrt{\tau^2 + \sigma^2}$. Which give $\sigma_0 = 32$ MPa and $\tau_0 = 22$ MPa. The resulting relations and the specimens above the 95th percentile (marked by circles) is shown in Fig. 17. Obviously, it is not possible to predict the failure of each individual test but such an approximate relation can give an indication on the behaviour of strong interfibre joints. Note that joints suffering from local stress concentrations or incomplete bonding within the interface are not predicted by the analysis.

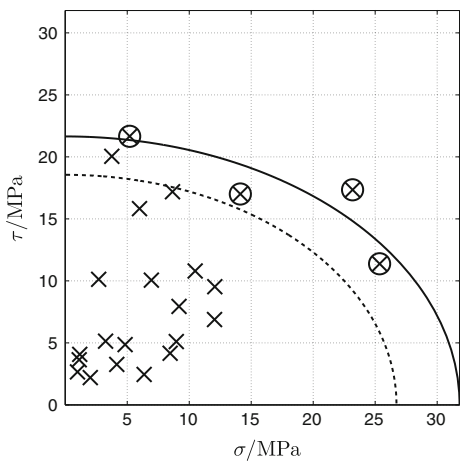

Fig. 17 The estimated effective normal stress is plotted against the effective shear stress at rupture. The estimated relation using all data is shown as a *dashed line* and the relation of the joints above the 95th percentile (indicated with *circles*) are shown as a *solid line*

Discussion

Despite the obvious approximations of the geometry, such as assuming the reference configuration to be planar, that the fibres are assumed to be prismatic, that kinks in the depth direction as well as micro compressions are neglected, there could be other sources of error introduced in the evaluation, such as the overlap area. It was argued by Kappel et al. (2009) that the regions close to the edge of the overlap region are not likely to form chemical bonding, also if holes or regions without bonding appear within the overlap it would certainly change the stress state in the fibre–fibre interface. Furthermore, as described above, the displacement at rupture in the simulations was not necessarily equal to the displacement at rupture of the tested specimen since the work of deformation was used to scale the model response to the experimental response; the resulting discrepancies are most likely due to errors in the determination of the fibre cross-section geometry.

Even though the force that was required to rupture the interfibre joint was lower than the force required to break the constituent fibres, progressive damage behaviour was sometimes seen in the experiments. This type of behaviour was sometimes indicated by a structural response that was not monotonically increasing. Such a sudden drop in force means that the physical contact area right before rupture cannot be assumed to be the same as in the initial configuration. Since the numerical model does not take any damage behaviour into account, such specimens could obviously not be analysed accurately in the present model, and were not subjected to further analysis.

Comparison of methods

In this study, the maximum force of the fibre–fibre cross was not assumed to be equal to the transferred force of the interfibre joint (as is commonly approximated in fibre–fibre joint testing) since most methods rely on a one-dimensional load cell, meaning that only the force in a certain direction is measured, neglecting the reaction forces due to a non-symmetric fibre–fibre cross. In this

study, a three-dimensional finite deformation was allowed for in the analysis and the model response was calibrated to the force and displacement measured by the miniature load cell and the extensometer. The direction of the maximum shear force was shown to not coincide with the direction of the applied loading (as is often assumed) and may introduce errors in the measured "shear strength value". Furthermore, an interfibre joint "shear test" has in this study been shown to pose significant out-of-plane moments in an opening mode of fracture combined with the sliding mode of fracture.

Calibration and model approximations

The structural model was based on a number of measurements of the fibre–fibre cross geometry but taking everything into account would have been both theoretically and practically impossible. The aim of this study was to develop a method of evaluation that is balanced in respect to the quantitative and the qualitative properties. In this study, the micro-fibril angle, wall thickness and width of the fibres (when the cross section was approximated as a rectangle with circular corners), the natural curvatures and kinks that spanned the image plane, a transverse isotropic material behaviour with engineering constants estimated from that of wood cells, finite rotations, the measured load at rupture and the total work of deformation, were all taken into account. It should be noted that other parameters may have an influence on the damage mechanism such are micro compressions, anisotropy, kinks or curvatures in the depth direction, pits or defects, but were not considered in the present study. The model was then in a sense inversely modelled, by using the stiffness of the first principal axis as a scaling parameter (that wound helically around the fibre) for both fibres, so that the approximations (mentioned above) and the force at rupture were maintained as well as minimising the work of deformation. So, the scaled stiffness may be thought of as a parameter that reduces the error due to the influence of the parameters that were not included in the model (since they may or may not have an influence on the structural response) so that a reasonable qualitative evaluation of the loading in the joint can be achieved with a reasonable number of estimations. Since the obtained values of this scaling parameter range over two orders of magnitude, it is possible that the influence of some deformation mechanism has been ignored. Moreover, a transversely isotropic material model is thought to better capture the behaviour of pulp fibres that are relatively weak in the direction transverse to the micro fibrils, compared to a fully isotropic model. Both models result in good agreement in terms of the structural response, however, the force and moments resultants differ about 40 % when analysed for two specimens (X3 and X10) with very low and very high micro fibril angles, respectively when compared between isotropic and anisotropic behaviour.

Scaled resultant forces and moments and the influence of the mode of loading

The evaluated resultant forces and moments indicate that the peeling moments are in general larger for specimens tested in a Mode I type of loading, but the amount of twisting moment that arises should somehow be controlled in order to obtain simpler stress states in the interfibre joints.

Since the fibre dimensions change and the true contact areas were unknown, rescaling of the resultant forces and moments to obtain a failure surface in terms of stress is difficult. The state of loading obtained at the centroid in terms of the scaled resultant quantities using the present approximations and assumptions reduced the scatter in the result, but did not clearly define a failure surface. This could indicate that the proposed method fails to take into account underlying structural properties such as partial bonding in the interface region, or simply that the strength of the chemically bonded regions varies considerable from specimen to specimen. It is interesting that the relative strength of the interfibre joints is, after taking the mode of loading into account are still varying. This result indicates that the interfibre joint strengths tested are not only influenced by the mode of loading (due to the geometry or the application of the load), but vary also from specimen to specimen.

A noteworthy feature was found when comparing the geometry in terms of κ_c or κ_l to the resultant forces and moments. As the tortuosity increases both the variations and the amplitude of the resultants decreases. A possible explanation is that when the amount of natural curvatures is increased, the mode of loading becomes more mixed and thus lowers the effective strength of the interfibre joint and as a more compliant structure allows for larger rotations of the interface, the specimens may fail in a weakest link manner while for low tortuosities, the structure is more restricted and thus a larger variation is introduced as the interface may or may not be loaded in the weakest orientation.

One interpretation is that there is an inherent property of the interfibre joints that was not taken into account in the evaluation, for example the relative bonded area, on the other hand, it was recently shown that the drying pressure has a negligible influence on the mean interfibre bond strength (Magnusson et al. 2013), indicating that a maximal (for that particular interfibre joint) relative bonded area is already obtained at low nominal drying pressures. Thus, either the surface roughness (which allows a certain relative bonded area to be obtained) yields a certain distribution of chemical bonding mechanisms (which vary in strength) for a certain interfibre joint, which in turn would result in a distribution of strengths with no influence of drying pressure, or there is a systematic error introduced in the experimental measurements. The latter could be that the joints are partially damaged prior to testing. Even though this cannot be ruled out, it is the authors' belief, that if this was the case, more complete failures during the mounting process would have been seen since the failure load should be very low for these specimens. In a recent paper, Persson et al. (2013) the surface roughness of fibres were studied and it was concluded that very close contacts are obtained due to capillary bridges pulling the wet and flexible fibres together during drying. Since both the hardness of the fibre surfaces and the stiffness of the cell wall layers are highly reduced when wet, the hypotheses that the effect of the drying pressure when preparing individual fibre–fibre crosses is negligible, is supported.

Note also that the evaluated resultants at failure are assumed to be independent of the temperature and moisture, which would influence the analysis.

Failure criteria

In the analysis, an approximate relation for the strength of the strong interfibre joints was estimated. Although not enough data were available to determine the true failure criterion, the estimated relation still serves as an approximate relation between the shear and normal stress that cause rupture. Note also, that similar relations are found if other specimens are used in the regression analysis (such as including only weak specimens), indicating that there is a certain failure criteria, but the strength of the individual specimens varies.

A natural direction for future research is to use a local failure criteria that takes into account the stress variations in the interface region, such as for example cohesive zone modelling, but that is beyond the objectives of this paper, which were to investigate how the global mode of loading influences the state of loading in the fibre–fibre interface in direct testing of interfibre joints.

Conclusions

A method for the evaluation of the stress-state in an interfibre joint test was developed. The load-displacement response of fibre cross specimens were fitted to structural models that take into account the initial geometry, microfibril angle, cell wall thickness, and large rotations. The state of loading at the fibre–fibre interface centroid then serves as an approximation of the state of loading in the interfibre joint. This state of loading was expressed in terms of two non-zero net force components, one normal to the interfibre joint surface and the other as the largest shear force parallel to the interfibre joint surface; and two non-zero moment components: one in-plane twisting moment about the interface surface normal describing a tearing mode of failure, and resultant out-of-plane moments describing peeling modes of loading of the interfibre joint. Furthermore, this paper has given qualitative examples and has introduced a method to evaluate how the geometry as well as the applied type of loading affect the mode of loading in the interfibre joints, as well as indications of the order of magnitude of the errors introduced when the initial geometry or large rotations are neglected in an evaluation of the interfibre joint strengths using direct methods. It was shown that the conventional failure criterion, assuming that the force at rupture is equal to the shear stress of the interfibre joint, tested in Mode II loading, only up to 23 % from the largest shear stress in the interfibre joint. Moreover, a relation taking also the normal force, and the twisting and opening moments into account have been estimated for the boundary of the interfibre joint strength of the samples tested. It was also shown that the magnitude of the twisting moments that arise in the fibre–fibre interface is of the same order as the peeling moment when tested in a Mode I type of loading. These results could be used to improve the methods used for testing interfibre joints to obtain more information on the strength components that are important for the build-up of strength in fibrous materials.

Acknowledgments The authors would like to acknowledge the financial support provided by BiMaC Innovation and the Swedish Research Council (Project Grant 2007-5380) and Professor Artem Kulachenko for all his helpful tips and suggestions.

Appendix

The climate and geometric properties for each evaluated specimen are tabulated in Tables 3 and 4.

Table 3 Specimen specific climate protocol

Specimen	Life/days	Temperature C/°	RH range/%
X1	1	22.0–23.8	17–29
X2	1	22.0–23.8	17–29
X3	0	23.8–23.9	21–21
X4	0	23.8–24.5	21–22
X5	0	24.3–24.4	23–23
X6	0	23.8–24.4	21–21
X7	0	24.3–24.4	23–23
X8	0	23.5–23.7	22–23
X9	0	23.5–24.1	21–23
X10	0	23.5–24.2	18–23
X11	0	23.8–24.1	23–24
X12	0	24.1–24.3	24–24
X13	0	24.3–24.4	24–25
X14	0	23.4–24.6	24–24
Z1	0	N/A	N/A
Z2	0	25.4–25.8	44–46
Z3	0	25.8–25.8	48–51
Z4	0	25.0–25.0	45–45
Z5	0	25.6–25.8	44–44
Z6	0	25.8–25.8	44–44
Z7	0	25.7–25.8	49–49
Z8	0	25.0–25.3	45–45
Z9	0	23.7–23.7	23–23

Table 4 Specimen geometry protocol

Specimen	w_c/ μm	w_l/ μm	t_c/ μm	t_l/μm	ψ_c/°	ψ_l/ °	e	κ_c	κ_l	E_1/GPa
X1	41	42	2.7	1.3	−22	−16	0.31	1.02	1.01	10.94
X2	27	53	3.8	3.7	−1	−1	0.25	1.01	1.01	1.59
X3	13	30	4.0	4.0	1	0	0.21	1.02	1.02	11.76
X4	25	36	3.5	1.4	−3	1	0.10	1.01	1.01	7.06
X5	32	29	3.5	3.7	−3	−4	0.49	1.00	1.00	4.49
X6	34	39	1.8	4.3	−26	3	0.44	1.04	1.04	6.96
X7	27	30	1.2	2.6	−3	−30	0.13	1.03	1.00	19.92
X8	32	30	4.0	3.0	2	−1	0.18	1.01	1.02	4.05
X9	78	33	3.8	3.0	−1	0	0.38	1.02	1.00	2.56
X10	32	16	1.3	1.4	−10	−26	0.22	1.03	1.01	3.40
X11	31	27	3.7	2.2	−2	−31	0.30	1.02	1.10	5.01
X12	39	23	3.8	4.3	−4	−5	0.43	1.03	1.07	0.10
X13	28	35	1.7	1.9	−26	−28	0.15	1.03	1.01	123

Table 4 continued

Specimen	w_c/ μm	w_l/ μm	t_c/ μm	t_l/μm	ψ_c/°	ψ_l/ °	e	κ_c	κ_l	E_1/GPa
X14	40	55	3.8	4.5	0	0	0.40	1.01	1.00	4.29
Z1	49	39	2.0	2.0	0	0	0.12	1.02	1.04	23.28
Z2	48	32	1.2	1.1	−17	−7	0.54	1.01	1.21	48.78
Z3	38	43	2.8	3.6	3	−7	0.65	1.12	1.04	1.12
Z4	49	49	4.0	4.0	1	3	0.45	1.01	1.00	67.56
Z5	38	27	1.3	3.9	−2	−1	0.56	1.01	1.02	85.36
Z6	29	45	1.9	3.8	−23	0	0.56	1.03	1.03	60.21
Z7	35	17	3.8	2.7	−2	−34	0.20	1.02	1.05	9.17
Z8	21	49	4.1	4.0	1	1	0.32	1.09	1.01	152.69
Z9	25	21	2.2	2.3	−5	−6	0.19	1.01	1.01	3.70

References

Abramoff MD, Magelhaes PJ, Ram SJ (2004) Image processing with imageJ. Biophotonics Int 11(7):36–42

Burgert I, Frühmann K, Keckes J, Fratzl P, Stanzl–Tschegg SE (2003) Microtensile testing of wood fibres combined with video extensometry for efficient strain detection. Holzforschung 57(6):661–664

Button AF (1979) Fiber–fiber bond strength—a study of a linear elastic model structure. Atlanta, Georgia

Corp DSS (2012) Abaqus/CAE. Dassault Systèmes

Dassault Systèmes Simulia (2012) Abaqus Analysis User's Manual, Dassault Systèmes

El-Hosseiny F, Page DH (1975) The mechanical properties of single wood pulp fibres: theories of strength. Fibre Sci Technol 8(1):21–31

Fengel D (1970) The physics and chemistry of wood pulp fibres. TAPPI J 8:74–99

Fischer WJ, Hirn U, Bauer W, Schennach R (2012) Testing of individual fiber–fiber joints under biaxial load and simultaneous analysis of deformation. Nordic Pulp Pap Res J 27(2):237–244

Groom LH, Shaler SM, Mott L (1995) Characterizing micro- and macromechanical properties of single wood fibres. International Paper Physics Conference. Niagara–on–the Lake, pp 11–14

Kappel L, Hirn U, Bauer W, Schennach R (2009) A novel method for the determination of bonded area of individual fiber–fiber bonds. Nordic Pulp Pap Res J 24(2):199–244

Lorbach C, Hirn U, Kritzinger J, Bauer W (2012) Automated 3D measurements of fiber cross section morphology in handsheets. Nordic Pulp Pap Res J 27(2):264–269

Magnusson MS, Zhang X, Östlund S (2013) Experimental evaluation of the interfibre joint strength of papermaking fibres in terms of manufacturing parameters and in two different loading directions. Exp Mech. doi: 10.1007/s11340-013-9757-y

Matlab (2012) R2012a. The MathWorks, Inc., Natick, MA

Mayhood CH, Kallmes OJ, Cauley MM (1962) The mechanical properties of paper—part II: measured shear strength of individual fiber to fiber contacts. Tappi J 45(1):69–73

McIntosh DC (1963) Tensile and bonding strengths of loblolly pine Kraft fibers cooked to different yields. Tappi J 46(5):273–277

Mohlin U (1974) Cellulose fibre bonding. Svensk Papperstidn 4(1):131–137

Neagu RC, Gamstedt EK, Lindström M (2004) Influence of wood–fibre hygroexpansion on the dimensional instability of fibre mats and composites. Compos Part A 36:772–788

Neagu RC, Gamstedt EK, Bardage SL, Lindström M (2006) Ultrastructural features affecting mechanical properties of wood fibres. Wood Mater Sci Eng 1:146–170

Nishino T, Takano K, Nakamae K (1995) Elastic modulus of the crystalline regions of cellulose polymorphs. J Polym Sci 33(11):1647–1651

Page DH (1960) Fibre-to-fibre bonds part 1—a method for their direct observation. Pap Technol 1(4):407–411

Page DH (1969) A method for determining the fibrillar angle in wood tacheids. J Microsc 90(2):137–143

Page DH, El-Hosseiny F (1974) The birefringence of wood pulp fibres and the thickness of the S1 and S2 layers. Wood Fiber Sci 6(3):186–192

Page DH, El-Hosseiny F, Winkler F, Lancaster APS (1977) Elastic modulus of single wood pulp fibres. Tappi J 60(4): 114–117

Persson K (2000) Micromechanical modelling of wood and fibre properties. L. University, Ed., Lund: Department of Mechanics and Materials

Persson BNJ, Ganser C, Schmied F, Teichert C, Schennach R, Gilli E, Hirn U (2013) Adhesion of cellulose fibers in paper. J Phys Condens Matter 25:1–11

Saketi P, Von Essen M, Mikczinski M, Heinemann S, Fatikow S, Kallio P (2011) A flexible microrobotic platform for handling microscale specimens of fibrous materials for microscopic studies. Microscopy 248(2):163–171

Schmied FJ, Ganser C, Fischer WJ, Hirn U, Bauer W, Schennach R, Teichert C (2012) Utilizing atomic force microscopy to characterize various single fiber–fiber bonds. International paper and coating chemistry symposium, pp 141–143

Schniewind AP, Nemeth LJ, Brink DL (1964) Fiber and pulp properties—1. Shear strength of single–fiber crossings. Tappi J 47(4):244–248

Stratton RA, Colson NL (1990) Dependence of fiber/fiber bonding on some papermaking varables. IPST Technical Paper Series, Institute of Paper Science and Technology, Atlanta, Georgia

Thorpe JL, Mark RE, Esufzai ARK, Perkins RW (1976) Mechanical properties of fiber bonds. Tappi J 59(5):96–100

Torgnysdotter A, Kulachenko A, Gradin P, Wågberg L (2007) Fiber/fiber crosses: finite element modeling and comparison with experiment. J Compos Mater 41(13):1603–1618

Ye C (2006) Spectroscopic imaging ellipsometry: real–time measurement of single, intact wood pulp fibers. Appl Opt 45(36):9092–9104

Ye C (2007) Spectroscopic imaging ellipsometry of wood fiber cell walls: a comparison with confical microscopy. Tappi J 6(8):26–32

Ye C, Sundström O (1996) Determination of S2–fibril–angle and fiber–wall thickness by microscopic transmission ellipsometry. Tappi J 80(6):181–190

Ye C, Sundström O, Remes K (1994) Microscopic transmission ellipsometry: measurement of the fibril angle and the relative phase retardation of single, intact wood pulp fibers. Appl Opt 33(28):6626–6637